

ENSO-like Interdecadal Variability: 1900–93

YUAN ZHANG, JOHN M. WALLACE, AND DAVID S. BATTISTI

Department of Atmospheric Sciences, University of Washington, Seattle, Washington

(Manuscript received 2 January 1996, in final form 18 June 1996)

ABSTRACT

A number of recent studies have reported an ENSO-like EOF mode in the global sea surface temperature (SST) field, whose time variability is marked by an abrupt change toward a warmer tropical eastern Pacific and a colder extratropical central North Pacific in 1976–77. The present study compares this pattern with the structure of the interannual variability associated with the ENSO cycle and documents its time history back to 1900. The analysis is primarily based on the leading EOFs of the SST anomaly and “anomaly deviation” fields in various domains and the associated expansion coefficient (or principal component) time series, which are used to construct global regression maps of SST, sea level pressure (SLP), and a number of related variables. The use of “anomaly deviations” (i.e., departures of local SST anomalies from the concurrent global-mean SST anomaly) reduces the influence of global-mean SST trends upon the structure of the EOFs and their expansion coefficient time series. An important auxiliary time series used in this study is a “Southern Oscillation index” based on marine surface observations.

By means of several different analysis techniques, the time variability of the leading EOF of the global SST field is separated into two components: one identified with the “ENSO cycle-related” variability on the interannual timescale, and the other a linearly independent “residual” comprising all the interdecadal variability in the record. The two components exhibit rather similar spatial signatures in the global SST, SLP, and wind stress fields. The SST signature in the residual variability is less equatorially confined in the eastern Pacific and it is relatively more prominent over the extratropical North Pacific. The corresponding SLP signature is also stronger over the extratropical North Pacific, and its counterpart in the cold season 500-mb height field more closely resembles the PNA pattern. The amplitude time series of the ENSO-like pattern in the residual variability reflects the above-mentioned shift in 1976–77, as well as a number of other prominent features, including a shift of opposite polarity during the 1940s.

1. Introduction

Time series of El Niño–Southern Oscillation (ENSO) indices such as the ones plotted in Fig. 1 exhibit a break or “regime shift” from 1976 to 1977, first noted by Quinn and Neal (1984, 1985) and in a more global context by Nitta and Yamada (1989). Subsequent studies of Trenberth (1990), Ebbesmeyer et al. (1991), Trenberth and Hurrell (1994), and Graham (1994) have emphasized the importance of this feature in relation to interdecadal climate variability over the North Pacific and parts of North America.

The difference maps shown in Fig. 2 summarize the features pointed out in the studies cited above. Time-mean SST has been higher in the later epoch 1977–93 over almost the entire tropical Pacific and off the west coast of the Americas, and it has been lower over the remainder of the extratropical Pacific. The pattern resembles the leading nonseasonal EOF of Pacific SST (Weare et al. 1976) and global SST (Hsuing and Newell

1983; Nitta and Yamada 1989; Parker and Folland 1991¹; Tokioka et al. 1995), which is reminiscent of the SST signature of ENSO. The signature of the Southern Oscillation is clearly evident in the sea level pressure (SLP) difference pattern, with higher pressure in the later epoch over the tropical western Pacific and Indian Oceans and lower pressure over the eastern Pacific. The change in the zonal SLP gradient across the equatorial central Pacific implies a weakening of the easterly trade-winds there, which is evident in Graham’s analysis.

The more recent epoch has also been marked by lower SLP over the North Pacific, accompanied by stronger westerlies along 40°N, which favor enhanced sea–air fluxes and lower SST. Consistent with the SLP changes, cold season 500-mb heights over the extratropical North Pacific have been lower, and the positive polarity of the Pacific–North American (PNA) pattern (Wallace and Gutzler 1981) has been prevalent. Wintertime land sur-

Corresponding author address: J. M. Wallace, University of Washington, Box 351640, Seattle, WA 98195-1640.
E-mail: wallace@atmos.washington.edu

¹ In Parker and Folland’s study it appeared as the second EOF. The leading EOF was identified with the general upward trend in SST in their 1900–88 dataset. In the shorter datasets examined by Hsuing and Newell (1949–79) and Nitta and Yamada (1950–87), SST did not exhibit as strong an upward trend.

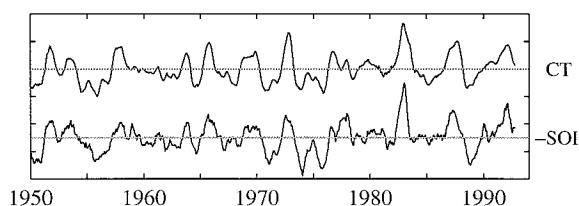


FIG. 1. Normalized monthly time series of the cold tongue index (CT) based on SST in the equatorial Pacific (6°S – 6°N , 180° – 90°W) and the conventional Southern Oscillation index (SOI) with sign reversed. Both time series have been smoothed with a 5-month running mean filter. The interval between tick-marks on the vertical axis is 1.0 standard deviation. Tick-marks on the time axis refer to January.

face air temperatures have been higher over Alaska and western Canada.

Most of the research on ENSO-like interdecadal variability has been based on the period of record from 1950 onward, in which the changes that occurred around 1976–77 are the outstanding feature. Cayan and Peterson (1989), Trenberth (1990), Trenberth and Hurrell (1994), and Francis and Hare (1994) have examined longer time series of indices of SLP over the extratropical North Pacific that provide an indication of the amplitude and polarity of the PNA pattern prior to the advent of upper-air analyses. These analyses indicate a pronounced shift toward higher SLP during the 1940s, concurrent with a shift toward higher SST in the central North Pacific (Fig. 11 of Dettinger and Cayan 1995) and higher wintertime surface air temperature at Alaska coastal stations (Fig. 3 of Francis and Hare 1994). The latter authors suggested that the SLP and surface air temperature changes were indicative of an abrupt shift in climate over the North Pacific, which was responsible for a decline in Alaskan salmon production. Time series presented in Shriver and O'Brien (1995) are indicative of a shift toward lower SST in the equatorial Pacific around the same time, accompanied by a strengthening of the Tradewinds in the equatorial central Pacific.

In the present study we will examine the global SST field and a selection of atmospheric fields and indices based on records dating back to the beginning of this century, including an index of the Southern Oscillation based upon marine surface observations. Following upon the recent studies of Tanimoto et al. (1993) and Zhang et al. (1996), we will explore the subtle distinctions between the structure of the interannual variability associated with the ENSO cycle² and the dominant pattern of variability on the interdecadal timescale. We will reexamine the changes that occurred around 1976–77

in light of these distinctions and compare them with other features in the record, such as the above-mentioned shifts in the 1940s. In contrast to many of the published studies on this topic, we do not presume that the decade-to-century scale variability can be separated from the interannual variability associated with the ENSO cycle by straightforward application of empirical orthogonal function/principal component (EOF/PC) analysis or related techniques. Accordingly, our analysis strategy relies upon 1) PC analysis of highpass- and lowpass-filtered SST fields as in Tanimoto et al. (1993), Wang (1995), and Yukimoto et al. (1996), (or, alternatively, regression analysis based on highpass- and lowpass-filtered versions of a reference time series); 2) analysis of the “residual SST field” from which the variability associated with the ENSO cycle has been removed by linear regression; and 3) comparison of the leading EOF of the SST anomaly fields in different geographical domains.

The paper is organized as follows. Data and analysis techniques are outlined in the next section. In section 3 we apply the three-part analysis strategy outlined in the previous paragraph to SST data for the period of record 1950–93. In section 4 we extend the analysis to the longer period 1900–93. To reduce the influence of the general upward trend in SST during the first half of the century upon the structure of the EOFs, we base the analysis in this section on the “SST anomaly deviation field” for each month: that is, the departure of the local SST anomaly from the global-mean SST anomaly. Section 5 documents in more detail the spatial signature of the interdecadal variability associated with the leading PC of the global SST anomaly deviation field, from which the signature of the ENSO cycle has been removed by linear regression, and compares it with the signature of the ENSO cycle. Section 6 provides a more detailed documentation of the interdecadal-scale variability as manifested in regional time series. The final section addresses a set of questions designed to elicit a synthesis and interpretation of the results.

2. Datasets and analysis procedures

The data used in this study are drawn from a number of different sources. With the one exception noted below, the marine surface observations are based on the Comprehensive Ocean–Atmosphere Data Set (COADS) (Fletcher et al. 1983), which comprises monthly mean fields on a 2° lat \times 2° long grid. The climatological mean for each calendar month was removed to obtain monthly anomalies, which were then averaged over 4° lat \times 6° long grid boxes centered at 0° , 4° , 8° ... lat and 0° , 6° , 12° ... long.

Monthly mean SST anomalies for the longer period of record 1900–93 used in sections 4 and 5 are based on an updated version of the quality controlled U.K. Meteorological Office Historical Sea Surface Temperature Dataset (Folland and Parker 1990, 1995), obtained

² For convenience, the term “ENSO cycle” will be used to refer to the interannual variability of the coupled atmosphere–ocean system in the equatorial waveguide, as described, for example, in Battisti (1988), Battisti and Hirst (1989), Latif et al. (1993), and Schneider et al. (1995). It is recognized that, in nature, the variations associated with the ENSO cycle are not strictly periodic.

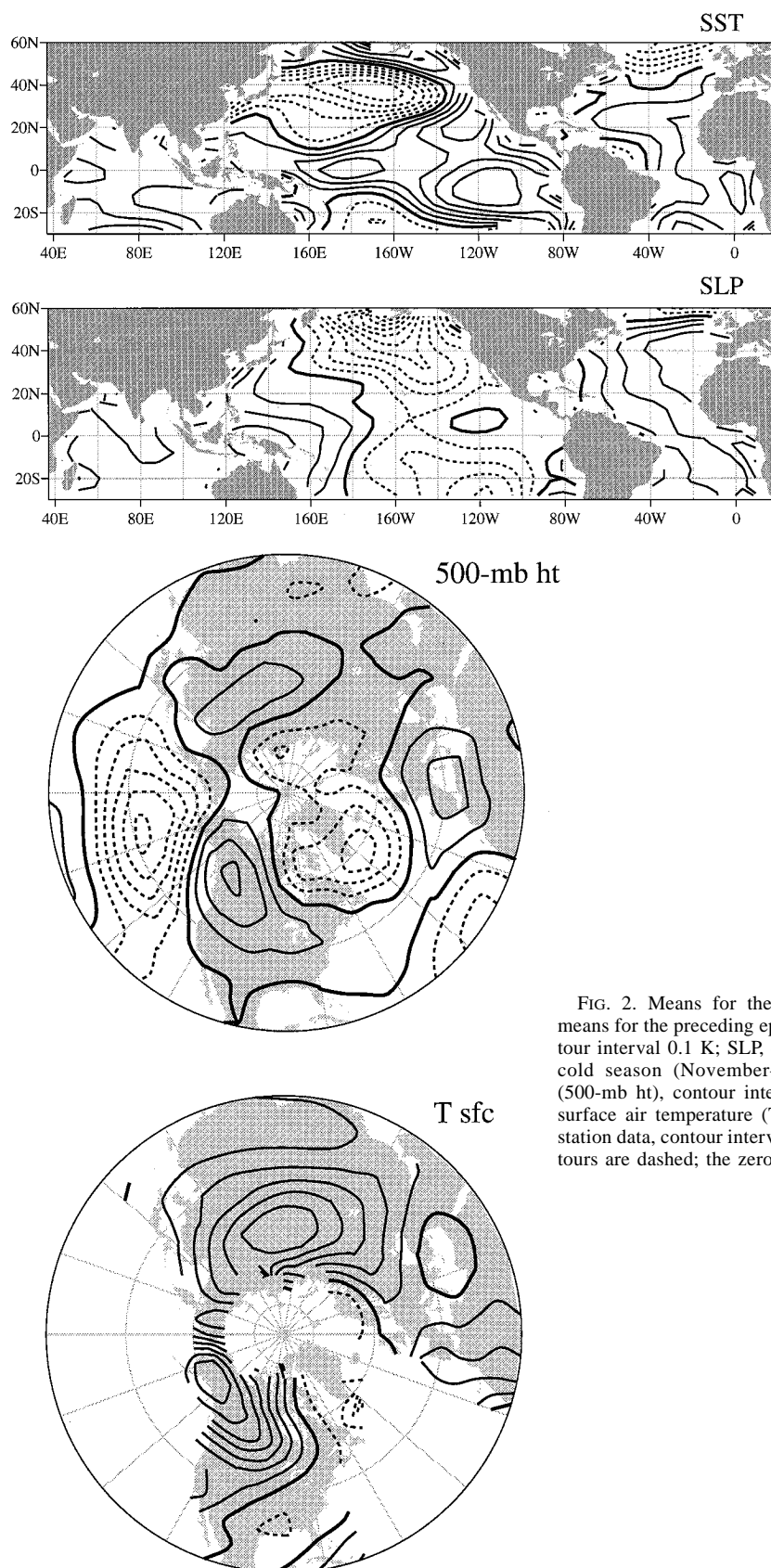


FIG. 2. Means for the epoch 1977–93 minus means for the preceding epoch 1950–76. SST, contour interval 0.1 K; SLP, contour interval 0.2 mb; cold season (November–April) 500-mb height (500-mb ht), contour interval 10 m; cold season surface air temperature (T sfc) based on gridded station data, contour interval 0.25 K. Negative contours are dashed; the zero contour is thickened.

from the Climatic Research Unit, University of East Anglia. The field is represented on a 5° lat \times 5° long grid, with grid boxes centered at 2.5° , 7.5° . . . lat and 2.5° , 7.5° . . . long. In the appendix, Table A3 provides an indication of the number of grid boxes contributing to the various SST indices used in this study, as a function of time. We have not attempted to make a formal quantitative determination of the adequacy of the sampling prior to 1920, but it can be inferred from the consistency of the time series based on different variables and different regions (Fig. 17 in section 7) that the sampling over the tropical oceans was adequate for the purposes of this study, and at least marginally adequate over the extratropical North Pacific, where the number of reports was much smaller.

Seasonal mean 500-mb height fields are based on National Meteorological Center (NMC, now known as the National Centers for Environmental Prediction) operational analyses, as described in Kushnir and Wallace (1989). Surface air temperature is represented by monthly 5° lat \times 10° long gridded fields based on station data, compiled under the sponsorship of the U.S. Department of Energy (Jones et al. 1985), and obtained from the Carbon Dioxide Information Analysis Center in Oak Ridge, Tennessee.

The EOF/PC analysis in this paper is based on the temporal covariance matrix, without any normalization. The maps shown in Figs. 3, 4, and 6 (later in this section) are formed by regressing the gridpoint values of the unfiltered SST anomaly fields upon the normalized PC time series. The contours on these maps have the same dimensions as the fields themselves, and their numerical values are indicative of the anomalies associated with typical (i.e., unit standard deviation) amplitudes of the mode in question.

In performing the EOF/PC analysis, missing grid points are simply ignored. Owing to the sparsity of data over much of the Pacific during the earlier decades of this century, as documented for example in Fig. 11 of Bottomley et al. (1990), the structure of the EOFs tends to be heavily influenced (and in the case of the tropical Pacific domain, dominated) by the variability during the second half of the century. In interpreting the variability during the earlier years, the PC time series can be viewed as indices, evaluated each month on the basis of whatever data happen to be available for that month.

The cold tongue index (CT), defined in the caption of Fig. 1 is the same as the one used by Deser and Wallace (1990). It is highly correlated with the more commonly used NINO-3 time series defined by Rasmusson and Carpenter (1982). Two monthly indices of the Southern Oscillation are used: the conventional one based on the difference between normalized Darwin and Tahiti SLP anomaly time series (Troup 1965, denoted SOI, obtained from the NOAA Climate Analysis Center) and a new COADS-based index (denoted SOI*), defined as the mean SLP anomaly in the tropical (20°S – 20°N)

Pacific from the dateline eastward, minus the mean SLP anomaly in the remainder of the tropical oceans (Atlantic, Indian, and western Pacific) based on all available data. The 5-month running mean SOI and SOI* time series are correlated with one another at a level of 0.87 based on the period of record 1950–93.

Use of an alternative COADS-based SOI* was motivated by our concerns about possible inhomogeneities in long station-based tropical SLP time series, in which a change as small as a few tenths of a millibar from one epoch to another due to undocumented changes in the observing protocol can be as large as the true interdecadal climate “signal.” An index based on marine surface observations is not necessarily any more reliable, but at least it provides an independent assessment of the interdecadal variability. That the SOI* time series tends to be more strongly correlated with the various SST-based time series considered in this paper than the conventional SOI time series (as documented in the bottom two rows of Tables A1 and A2 in the appendix) attests to its reliability.

The number of $2^\circ \times 2^\circ$ grid squares that contributed to the two poles of the SOI* each month is summarized in Table A4 (in the appendix). The lack of observations during World War I precludes the possibility of extending the record through that interval. However, the comparison with SST data presented in Fig. 16 (in section 6) indicates that the sampling prior to World War I, though sparse in comparison to later decades, was adequate to define the major excursions in the index.

The 6-yr lowpass-filtered time series were generated by successive applications of centered 25- and 37-month running means. Corresponding 6-yr highpass-filtered series were formed by subtracting the 6-yr lowpass-filtered time series from the original series. This procedure yields acceptably small negative sidelobes in the frequency response curve without sacrificing an undue number of data points at the ends of the time series.

3. Analysis for the period 1950–93

In this section, we will apply the three different analysis strategies outlined in section 1 to the COADS data for the period 1950–93. Results are presented in Figs. 3–7 and Tables 1 and 2.

The top panel of Fig. 3 shows the leading principal component (PC) time series based on the 6-yr highpass- and lowpass-filtered SST fields over the Pacific domain. The former captures virtually all the variability associated with the ENSO cycle, whereas the latter captures the break around 1976–77. The two series are weakly correlated with one another ($r = 0.20$, where r denotes the correlation coefficient), owing to the overlap between the frequency response of the filters. The PC based on the highpass-filtered SST data is highly cor-

TABLE 1. The difference between the temporal means for the periods of 1977–93 and 1960–76 for each time series shown in Fig. 5 in K (per standard deviation)⁻¹.

	(1977–93)–(1960–76)
CT	0.54
TP	0.80
G	1.09
G-TP	1.43
NP	1.12

TABLE 2. Numbers to the left of the slash marks are the temporal correlations between the time series shown in Fig. 5 (CT, TP . . .) and PCs of 6-yr highpass and lowpass filtered SST shown in Fig. 3. Numbers to the right of the slash marks are the corresponding spatial correlations based on the global regression patterns shown in Fig. 6.

	Highpass PC	Lowpass PC
CT	0.92/0.99	0.41/0.81
TP	0.90/0.97	0.56/0.85
G	0.88/0.95	0.61/0.89
G-TP	0.39/0.74	0.62/0.94
NP	0.38/0.73	0.64/0.95

related with the highpass-filtered cold tongue index time series ($r = 0.95$).

The spatial signatures obtained by regressing the global SST field upon the highpass- and lowpass-filtered PC time series are shown in the lower panels of Fig. 3, labeled as HP and LP, respectively. The two patterns are qualitatively similar, with large SST anomalies in the tropical Pacific, anomalies of opposite polarity in the extratropical central North Pacific, and a high degree of equatorial symmetry. (The spatial correlation between them, based on the full global domain, is 0.75.) The equatorial maximum in the eastern Pacific is more pronounced and more narrowly confined along

the equator in HP, whereas the SST fluctuations in the extratropical central North Pacific are more prominent in LP.

Patterns very similar to those in Fig. 3 can be obtained simply by regressing the unfiltered global SST field upon highpass- and lowpass-filtered versions of the cold tongue index or the Southern Oscillation index (not shown). Wang (1995) and Yukimoto (1996) obtained qualitatively similar patterns based on quite different filtering protocols.

Figure 4 shows the leading PC time series of the

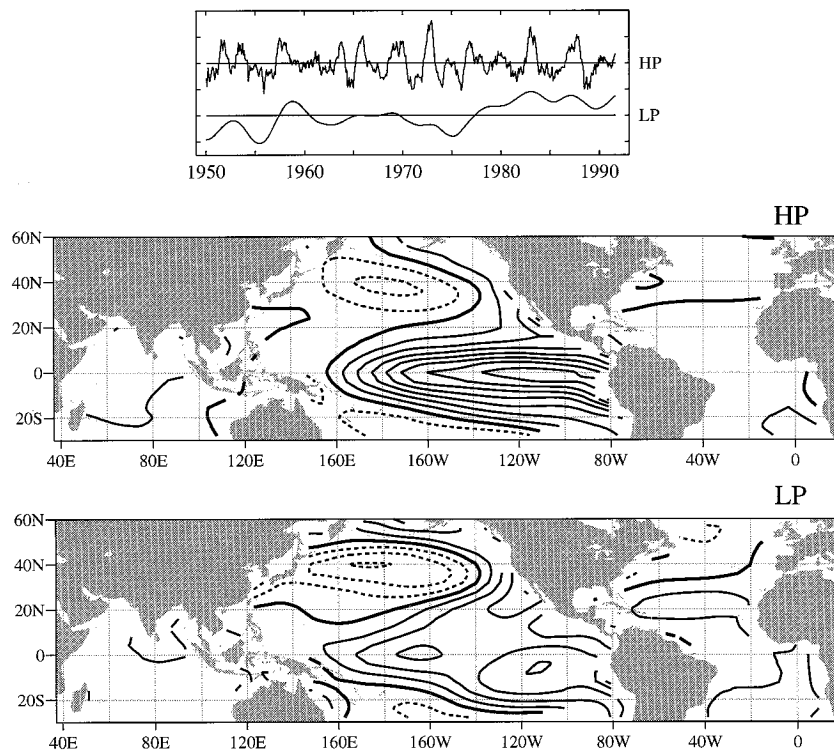


FIG. 3. The leading (normalized) PCs of 6-yr highpass- (HP) and lowpass- (LP) filtered SST over the Pacific domain shown together with the associated regression patterns for global SST. The interval between tick-marks on the vertical axis of the top panel corresponds to 1.0 standard deviation, and the spacing between the curves is arbitrary. Contour interval 0.1 K per standard deviation of the expansion coefficient time series. Negative contours are dashed; the zero contour is thickened.

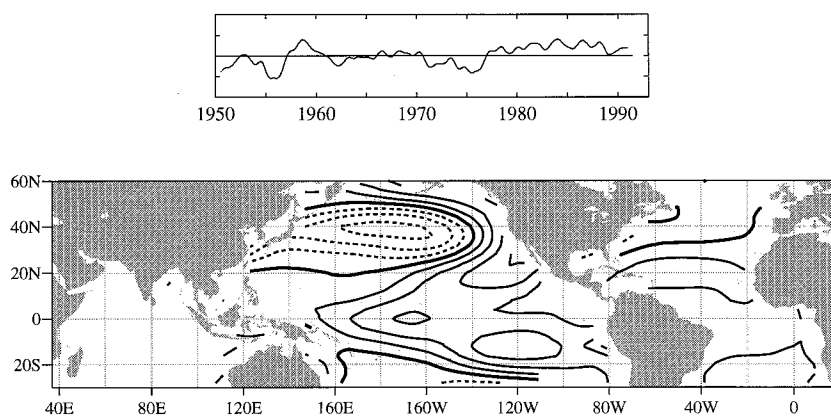


FIG. 4. The leading (normalized) PC of the residual SST field over the Pacific domain, from which the least-squares best fit to the time series of 6-yr highpass filtered cold tongue index at each grid point has been removed, shown together with the associated regression patterns for global SST. Contouring conventions as in the previous figure.

“residual SST anomaly field” for the Pacific basin. The residual time series at each grid point was formed by 1) regressing the monthly SST anomaly time series for the period 1950–93 upon the 6-yr highpass-filtered cold tongue index time series (hereafter denoted CT*); 2) multiplying CT* by the regression coefficient to obtain a “fitted time series”; and 3) subtracting this fitted time series from the original one. Although it contains somewhat more high-frequency variability, this PC time series is highly correlated with the lowpass PC in the previous figure ($r = 0.94$) and the corresponding regression patterns are even more strongly correlated in space ($r = 0.99$). The striking similarity between the regression pattern in Fig. 4 and the difference pattern shown in Fig. 2 suggests that this “modal structure”

might merely be a reflection of the changes that took place around 1976–77. However, the fact that a similar pattern (not shown) can be recovered by repeating the analysis on the segment of the record ending in December 1976 proves that this is not the case.

A family of patterns with contrasting characteristics reminiscent of those in Figs. 3 and 4 emerge as regression patterns for the leading PCs of unfiltered monthly SST anomaly fields in the following domains:

- TP: the tropical Pacific, defined as the region 20°N – 20°S , 160°E – 80°W ;
- G: the entire global ocean as represented by all available gridpoints as in Parker and Folland (1991);

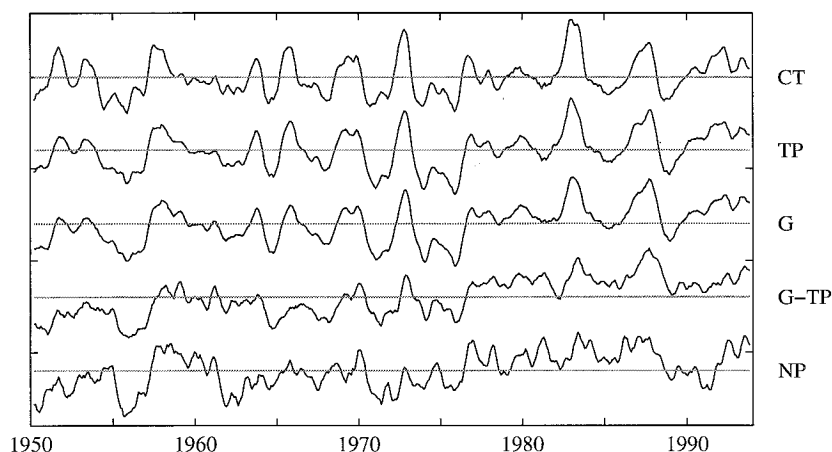


FIG. 5. Normalized time series (top to bottom): cold tongue (CT) and expansion coefficients of the leading EOFs of the SST anomaly field over the tropical Pacific (TP) domain (20°S – 20°N , 160°E – 80°W); the global (G) domain; the global domain excluding the TP ($G - TP$); and the extratropical (NP) domain poleward of 20° . All time series have been smoothed with a 5-month running-mean filter. The interval between tick-marks on the vertical axis is 1.0 standard deviation. The spacing between the curves is arbitrary. Correlation coefficients between the time series are shown in Table A1 in the appendix.

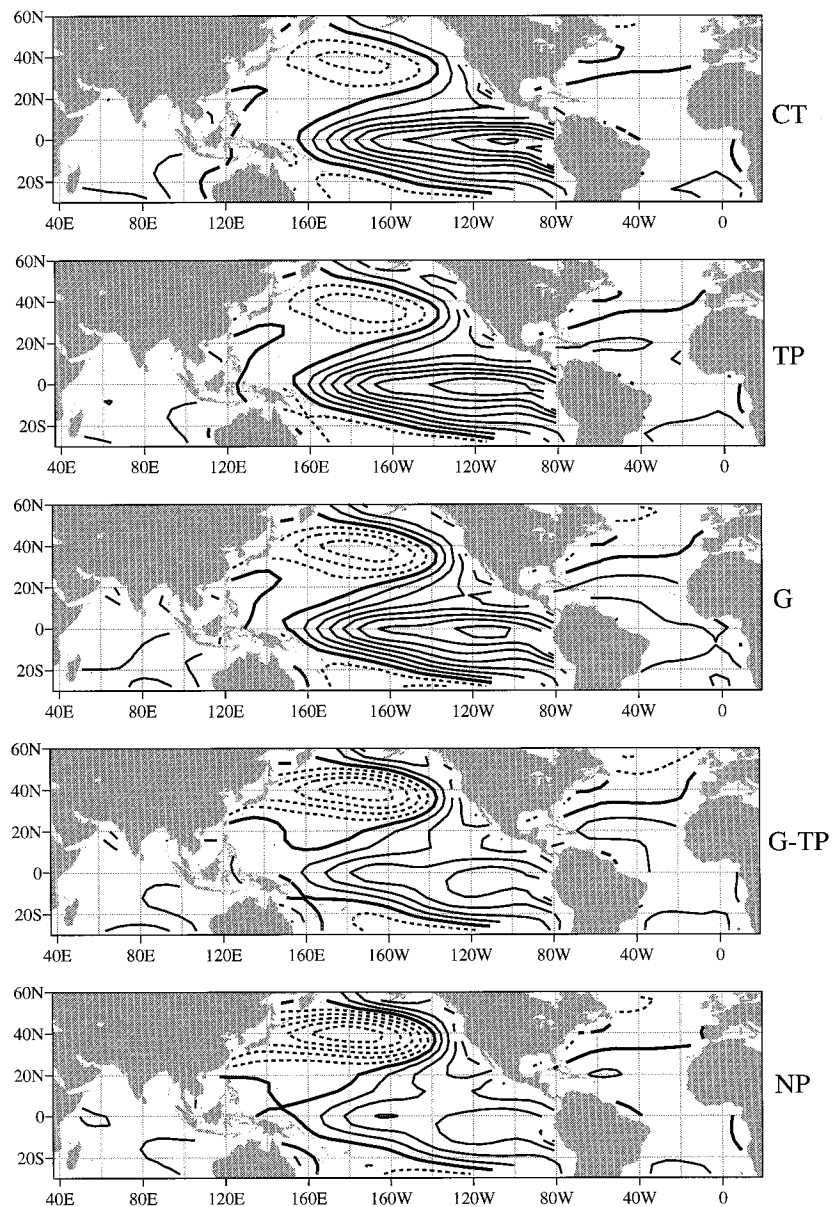


FIG. 6. Spatial patterns generated by regressing the global SST field upon the time series shown in the previous figure. Contour interval $0.1 \text{ K (standard deviation)}^{-1}$ of the corresponding time series. Negative contours are dashed; the zero contour is thickened.

G – TP: the entire global ocean exclusive of the tropical Pacific region TP;

NP: the extratropical North Pacific poleward of 20°N as in Davis (1976), all of whose eigenvalues are well separated from succeeding ones according to the criterion of North et al. (1982). The PCs are shown in Fig. 5, together with the time series of the cold tongue index (denoted by CT; repeated from Fig. 1), and the regression patterns are shown in Fig. 6.

The time series exhibit a number of common features.

The interannual variability associated with what we have termed “the ENSO cycle,” with major warm events in 1958, 1966, 1973, 1983, 1987, and 1992–93 is apparent in all of them but it becomes less prominent as one progresses downward from CT to NP. All the time series also exhibit a transition from a colder epoch 1960–76, to a warmer epoch starting in 1977, which becomes more pronounced as one progresses from CT to G – TP and NP. This evolution is clearly evident in the differences between the means for the epochs 1977–93 and 1960–76, summarized in Table 1.

The relationships between the 6-yr highpass and low-pass PCs shown in Fig. 3 and the unfiltered series in Fig. 5 are documented in Table 2. As one progresses from CT to NP, the correlation with highpass-filtered PC drops off sharply, reflecting the declining prominence of the ENSO cycle. In contrast, lowpass-filtered PC appears to be almost equally well correlated with all the time series in Fig. 5 (except with CT).

As one progresses from the upper to the lower panels of Fig. 6, the anomalies in the primary positive “center of action” over the equatorial Pacific become less equatorially trapped, and the negative anomalies in the extratropical Pacific become relatively more pronounced. Even though no filtering was involved in producing these patterns, this progression is reminiscent of the distinctions between the highpass and lowpass patterns in Fig. 3, as verified by the spatial correlation statistics presented in Table 2. Taken together, the results in Figs. 2–6 are indicative of a distinction between the predominantly local equatorial Pacific signature that characterizes the ENSO cycle and the more complex global structure that characterizes the interdecadal variability.

Figure 7 shows the cross-correlation function between CT and each of the other time series in Fig. 5. The lag is barely perceptible for TP and G and it increases to about a season for G – TP and NP, confirming that on the interannual timescale the remote features in the patterns shown in Fig. 6 are occurring in response to the ENSO cycle rather than as an integral part of it, consistent with the conclusions of Alexander (1992a,b) and Yulaeva and Wallace (1994).

4. Analysis for the period 1900–93

In this section we apply the same three analysis strategies as in the previous section to the U.K. Meteorological Office dataset for the longer period of record 1900–93 but in reverse order, starting with EOF analysis for the various spatial domains.

When Parker and Folland (1991) performed conventional EOF/PC analysis on the global SST field based on the longer period of record 1900–90, their leading mode was dominated by the upward trend in global mean SST prior to the 1940s. The mathematical constraint that subsequent PCs be orthogonal to this “global warming mode” seems physically unrealistic. To circumvent this problem, the PC analysis for the TP, G, G – TP, and NP domains in this subsection is performed on the *SST anomaly deviation field*

$$\text{SSTA}^*_{x,y,t} = \text{SSTA}_{x,y,t} - [\text{SSTA}]_t,$$

that is, the deviation of the SST anomaly at each grid point x, y from the global-mean $[(\)]$ SST anomaly for that same month t . In this formalism, the PCs are not subject to any orthogonality constraints with respect to the time series of global-mean SST. In fact, the leading PC of the global SST anomaly deviation field is posi-

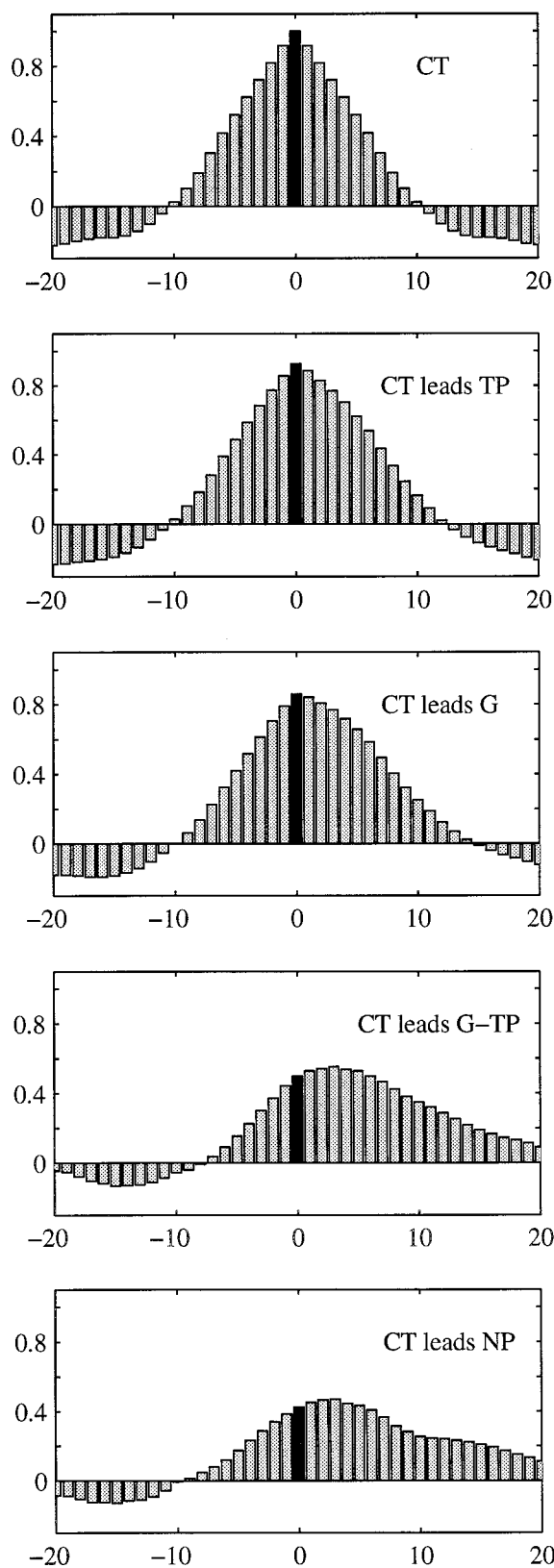


FIG. 7. Cross-correlation functions between the cold tongue index and the time series in Fig. 5, based on unfiltered data. The x axis represents the lag in months, where positive values indicate that CT is leading the other time series.

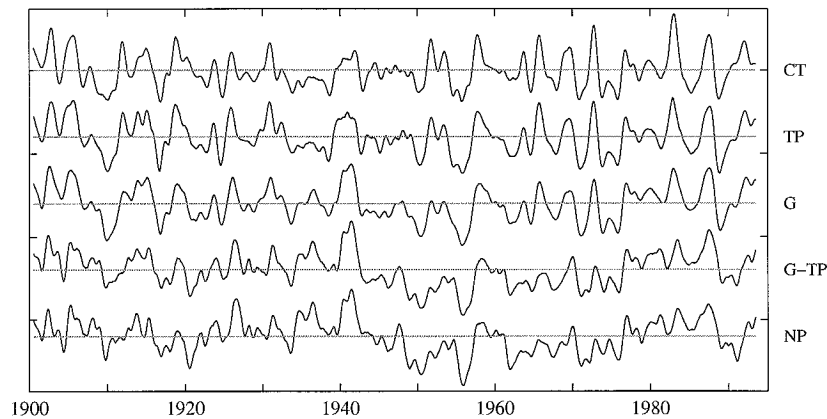


FIG. 8. As in Fig. 5, but based on the SST anomaly deviation field for the longer period of record 1900–93. All time series have been smoothed with successive 9-month and 5-month running-mean filters. The interval between tick-marks on the vertical axis is 1.0 standard deviation. The spacing between curves is arbitrary. Correlation coefficients between the time series are shown in Table A2 in the appendix.

tively correlated with global-mean SST at a level of nearly 0.7.

The leading PC time series for the global SST domain G, plotted as the third time series in Fig. 8, is consistent with its counterpart in Fig. 5 based on the shorter period of record: the correlation between them based on unsmoothed data for the overlapping period of record is 0.94 and the corresponding regression pattern (not shown) is virtually identical to its counterpart in Fig. 6.

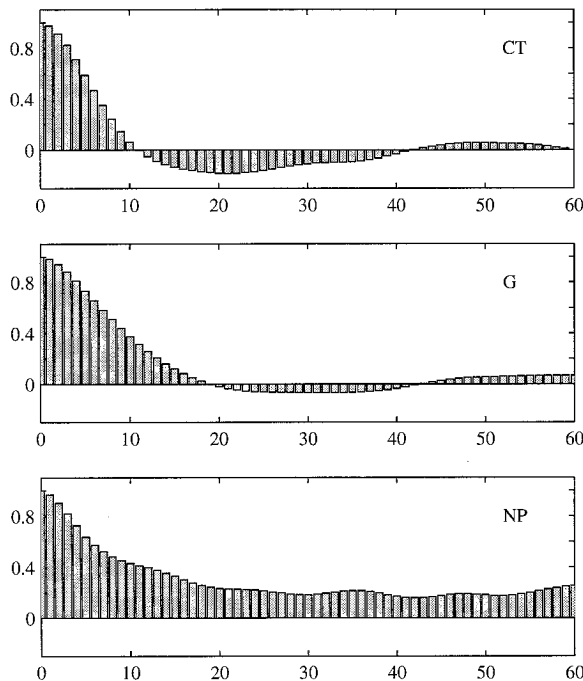


FIG. 9. Autocorrelation functions for three of the time series in Fig. 8, as indicated, based on 5-month running-mean data. The x axis represents the lag in months.

It is notable that the high mean value of this “G” time series during the post-1977 epoch is not unprecedented: the 1925–42 epoch averaged just about as high, and 1943–76 averaged substantially below the mean of the 94-yr record.

The other time series in Fig. 8 indicate the extent to which fluctuations in various parts of the World Ocean contribute to the features in the G time series. Rises in 1976–77 and falls in the 1940s are evident in all of them: they are most prominent in the leading PCs for the G – TP and NP domains and least prominent in the cold tongue index time series CT. Interannual features common to the tropical and extratropical time series include the dips centered around 1910, 1918, 1956, and 1989 and the pronounced peak in 1940–41. Some of these common features like the 1989 dip are relatively more pronounced in the TP series, while others like the sharp rise in 1958 are most pronounced in the NP series.

In summary, of the time series in Fig. 8, CT is most strongly dominated by the interannual variability associated with the ENSO cycle, while G – TP and NP exhibit the clearest evidence of interdecadal variability. This distinction is also evident in the autocorrelation functions shown in Fig. 9: CT’s negative sidelobe reflects the ENSO cycle, while NP’s positive values out to lags of 5 yr and beyond reflect the relatively greater prominence of the interdecadal variability.

5. Structure of the residual variability

In this section we will attempt to distinguish between the structure of the interannual variability associated with the ENSO cycle, and the interdecadal variability inherent in the G time series that is linearly independent of the ENSO cycle. As in the previous section, we will

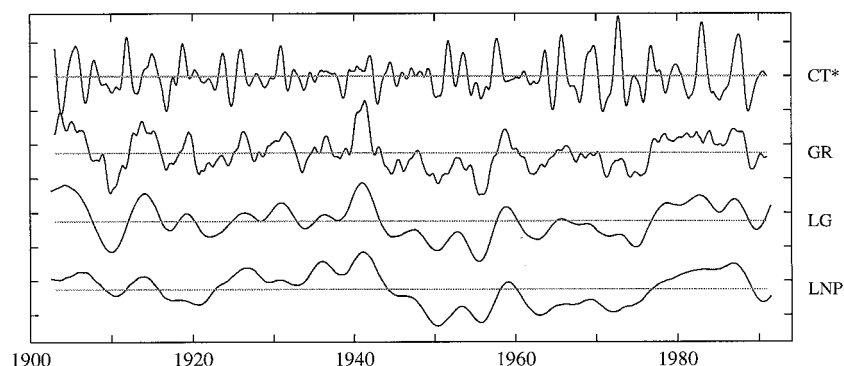


FIG. 10. Normalized time series. Here, CT* is the 6-yr highpass-filtered cold tongue index, GR is the residual of the G time series in Fig. 8 after the least-squares best fit to the CT* time series has been removed, LG is 6-yr lowpass-filtered G, and LNP is 6-yr lowpass-filtered NP. Smoothing and plotting conventions as in Fig. 8.

use the term “ENSO cycle-related” variability to denote the component whose time variations are linearly proportional to the 6-yr highpass-filtered cold tongue index time series CT*. The CT and CT* time series are highly correlated ($r = 0.94$), but the distinction between them is important in the context of this section because we wish to exclude from the reference time series for the ENSO cycle all interdecadal variability, regardless of whether it might be ENSO-related.

The CT* time series was linearly fitted, by the method of least squares, to the G time series in Fig. 8, and the fitted time series was subtracted from the original one to obtain the “residual time series” GR shown in Fig. 10. The interdecadal variability stands out more clearly in the residual time series, though some interannual variability is still present. The time series labeled LG in the figure was obtained by applying a 6-yr lowpass filter on the G time series. Despite their somewhat different visual appearances, GR and LG are correlated at a level of 0.93. The 6-yr lowpass-filtered NP time series (LNP) is also very similar.

The global SST, wind stress, and SLP fields were regressed upon GR to obtain the patterns in Fig. 11. The strong resemblance between these regression patterns and the corresponding difference maps in Fig. 2 establishes that the changes that took place in 1976–77 are characteristic of the dominant pattern of the interdecadal variability associated with GR. It is also instructive to compare them with their counterparts based on CT*, shown in Fig. 12, which can be viewed as representative of the ENSO cycle. Considering that the anomaly patterns in Figs. 11 and 12 are based on reference time series that are linearly independent of one another, the degree of similarity between them is quite remarkable: both could be described as “ENSO-like.” The most obvious distinction between them is the higher amplitude of the equatorial Pacific features in Fig. 12. The wind stress anomalies, in particular, are much stronger and more suggestive of a general increase in the strength of the lower branch of the Hadley

circulation across the entire Pacific sector, consistent with the prominent equatorial minimum in the SLP anomalies in the central Pacific. In contrast, in Fig. 11 the meridional SLP gradient is weak and the equatorward wind stress anomalies appear to be in geostrophic balance with the east–west gradient of the SLP anomalies. The stronger convergence over the equatorial Pacific in the pattern based on CT* is suggestive of stronger rainfall anomalies in association with the ENSO cycle.

The corresponding regression maps for the cold season 500-mb height (1946–93) and surface air temperature (1900–90) fields are shown in Figs. 13 and 14, respectively. The 500-mb height pattern based on GR more closely resembles the PNA pattern, whereas the one based on CT* is more similar to the correlation patterns in Horel and Wallace (1981). The most prominent differences between the patterns are over Canada, where the positive regression coefficients extend farther eastward in the pattern based on CT*. The minor distinctions between the surface air temperature patterns based on GR and CT* are consistent with the differences between the corresponding 500-mb height patterns. For example, the positive regression coefficients in the pattern based on CT* extend farther to the east across southern Canada and the northern United States. The agreement between the 500-mb height and surface air temperature patterns also illustrates the consistency between the results based on the periods of record 1946–92 and 1990–92.

The extratropical response to ENSO is largely a cold season phenomenon (Horel and Wallace 1981; Webster 1982). To determine whether the same is true of the residual ENSO-like variability, the regression calculation that was used to generate Figs. 11 and 12 was repeated with the monthly data stratified by boreal cold and warm season. The resulting regression patterns (not shown) indicate that the extratropical SST signature is observed year-round, whereas the extratropical response in the SLP field is largely restricted to the cold season,

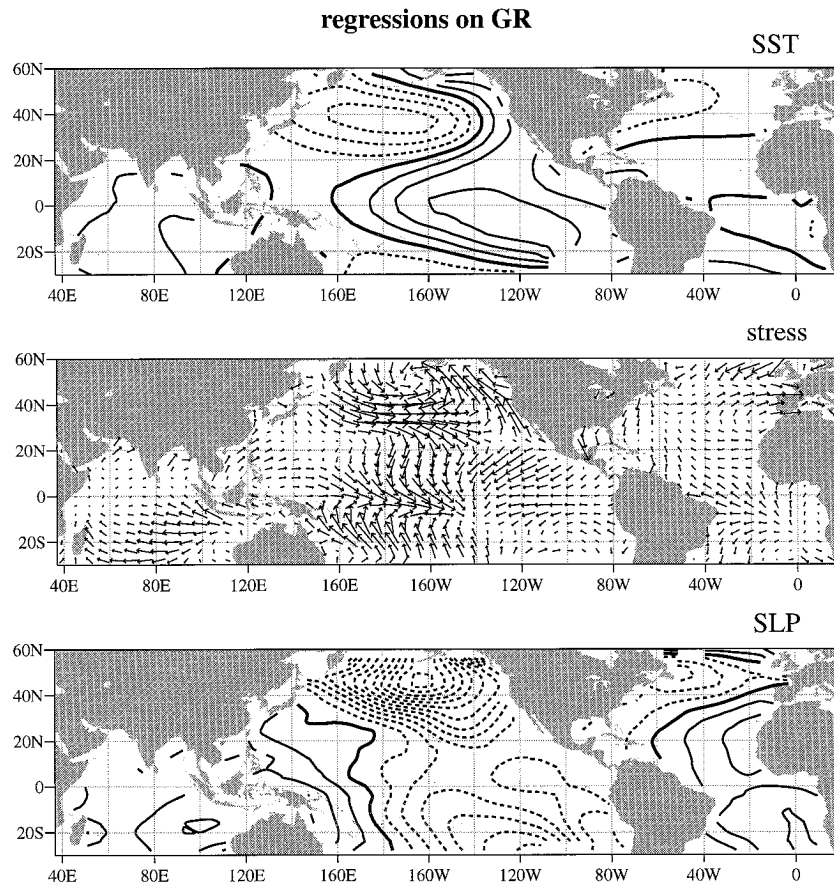


FIG. 11. Global fields regressed upon the time series labeled GR in Fig. 10: (top) SST, contour interval $0.1 \text{ K [standard deviation (std)]}^{-1}$; (middle) wind stress, the longest vectors represent a value of $8.3 \text{ m}^2 \text{ s}^{-2}$ per std; (bottom) SLP; contour interval $0.1 \text{ mb (std)}^{-1}$. The negative extremum in the vicinity of the Aleutian Low corresponds to $1.3 \text{ mb (std)}^{-1}$. Negative contours are dashed; the zero contour is thickened.

when it is roughly twice as strong as in Figs. 11 and 12. Even the tropical manifestation of the Southern Oscillation appears to be somewhat stronger during the boreal cold season.

The calculations in this section were repeated, using LG and LNP as reference time series in place of GR. The leading PC of the residual SST anomaly deviation field in the Pacific domain from which the least-squares best fit to CT* at each grid point had been removed was also used. In all cases, the resulting regression patterns turned out to be very similar to those shown in Fig. 11 and the left-hand panels of Figs. 13 and 14.

6. Regional manifestations of interdecadal variability

It is of interest to determine whether the changes that occurred during the 1940s exhibited a spatial signature similar to the ones that occurred during the 1970s, documented in Fig. 2. Figure 15 shows the difference in the SST anomaly deviation and SLP fields: the epoch 1943–76 minus the previous epoch 1925–42, which can

be compared with their counterparts in the first two panels of Fig. 2. Apart from the polarity reversal, the overall similarity of the patterns is quite remarkable. The most notable discrepancy is the weaker Southern Oscillation signature in the tropical SLP field, particularly on the western (Australian) side of the “see-saw.” The regional time series in Fig. 16 provide a more detailed documentation of the variability over the full 94-yr record. In agreement with the previous figure, the early 1940s were marked by a rise in SST in the central North Pacific (CNP), which appears as a drop in the inverted time series shown in the figure and cooling in the eastern North Pacific (ENP). SST in the Indian Ocean (IND) and the eastern tropical Pacific (ETP) leveled off after a 20-yr rising trend and these regions cooled relative to global-mean SST. These changes are all in the opposite sense as the ones that occurred around 1976–77. However, SLP at Darwin and, more generally, to the west of the dateline (not shown) did not drop relative to the previous decade as might have been expected, and the cooling in ENP occurred later and much more gradually than the rise in CNP. Hence, it cannot

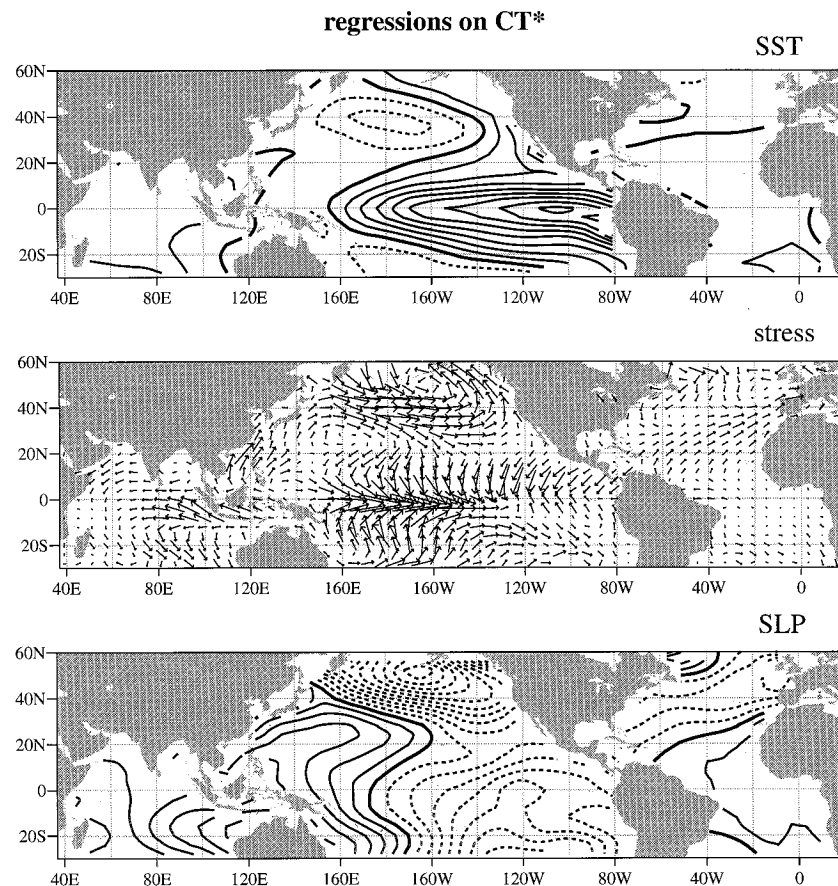


FIG. 12. As in Fig. 11, but based on CT* in Fig. 10.

be said that the 1942–43 changes are perfectly analogous to the ones that occurred in 1976–77. A better analog is the suite of abrupt changes that took place from 1957 to 1958.

7. Discussion

In this final section we will draw upon the observational results presented above to address a set of questions designed to explore the relationship between the ENSO cycle and the ENSO-like interdecadal variability, as exemplified by the changes that took place in 1976–77.

Are the changes that occurred in 1976–77 of singular importance in the context of the 94-yr record examined in this study? The time series in Fig. 8 and many of the ones in Fig. 16 exhibit analogous changes, but in the opposite direction around 1942–43. A selection of the series in Fig. 8 are shown again in Fig. 17, together with two SLP indices: NPP, a measure of SLP averaged over the extratropical central North Pacific, which is similar to the indices used by Cayan and Peterson (1989), Trenberth (1990), and Trenberth and Hurrell (1994); and SOI*, the COADS-based Southern Oscillation index described in section 2. Both indices are shown inverted to make their time series positively cor-

related with the SST time series. Also shown is the time series of AC, an index of surface air temperature over Alaska and western Canada. A rise in the mean values of all the indices occurred around 1976–77 and a drop occurred during the 1940s. Conditions during the 1977–93 epoch are reminiscent of those that prevailed during the epoch 1925–42.

It would be a gross oversimplification to characterize the ENSO-like residual variability of the global SST field solely in terms of such interdecadal “regime shifts,” which become apparent only with the benefit of hindsight. The changes that occurred around 1957–58 were no less dramatic than the ones around 1976–77: they have received less emphasis here and in other papers simply because the subsequent warm epoch in the tropical Pacific persisted for only a few years. It is too early to tell whether the warming that took place in 1990–91, documented by Mantua and Graham (1997, manuscript submitted to *J. Climate*), will persist long enough to become famous. Regardless of whether it does, features such as these are no less important in terms of the climate assessment, diagnosis, and prediction than the two features singled out for emphasis in the present study.

As argued by Dettinger and Cayan (1995), the notion

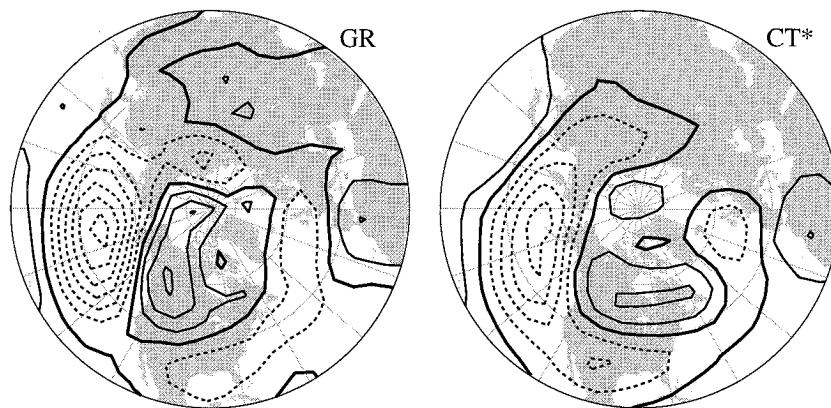


FIG. 13. Cold season (November through April) 500-mb height field for the period of record 1946–93 regressed upon GR and CT*, as indicated. Contour interval 5 m (std)^{-1} ; negative contours are dashed; the zero contour is thickened.

of discrete “regime shifts” may not be the most informative way of characterizing climatic variability over the North Pacific. Indeed, the GR time series in Fig. 10 could equally well be interpreted as being characterized by a pronounced cooling trend from 1943 to 1955, followed by a more gradual warming trend extending nearly until the end of the record.

How should the leading EOF of the global SST field (G) be interpreted? It is evident from Tables A1 and A2 in the appendix that the Southern Oscillation indices SOI and SOI* are more strongly correlated with G than with CT. The correlation between G and SOI* (~ 0.9) is particularly impressive in this respect. Hence, the leading EOF of the global SST field is closely associated with the Southern Oscillation but less so with the “El Niño” component of ENSO. It is perhaps worth noting that the leading EOF of SST over the Pacific basin alone yields a spatial pattern that is virtually identical to the Pacific portion of G .

Are the subtle distinctions between the structures of the “ENSO cycle-related” (CT) and “residual” (GR)*

variability in Figs. 11 and 12 of any physical significance? The more strict confinement of the higher frequency fluctuations to the equatorial waveguide appears to be a robust result. The fact that these distinctions are mirrored in Fig. 3, which was constructed from 6-yr highpass- and lowpass-filtered SST fields, suggests that they might be related to the frequency dependence of the atmosphere–ocean coupling in the equatorial waveguide. Consider, for example, the different patterns of thermocline displacements resulting from forcing the equatorial Pacific with a patch of zonal wind stress anomalies near the dateline, oscillating at various frequencies. Westerly wind stress anomalies near the dateline will act to deepen the thermocline in the eastern Pacific. The poleward and westward extent of the thermocline anomaly increases as the frequency of the forcing decreases because Rossby energy emanates from the eastern boundary at higher latitudes (Clarke 1983) and travels westward at a more shallow angle as the frequency of the incident Kelvin signal is decreased. Thus, a decrease in the frequency of the wind stress anomaly

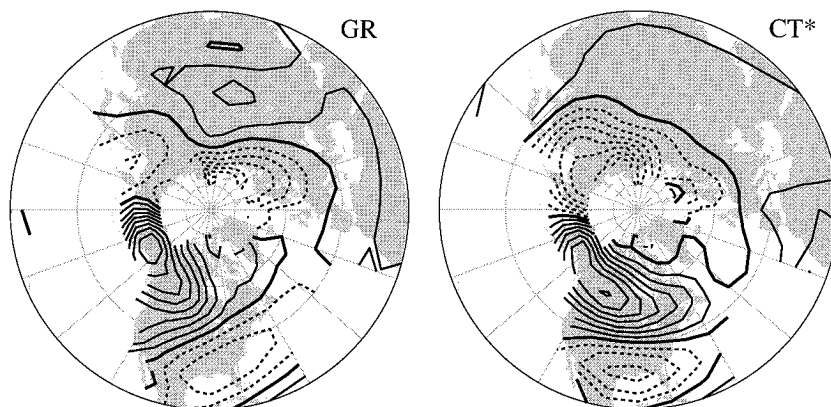


FIG. 14. Cold season surface air temperature field for the period of record 1900–93 regressed upon GR and CT*, as indicated. Contour interval 0.1 K (std)^{-1} ; negative contours are dashed; the zero contour is thickened.

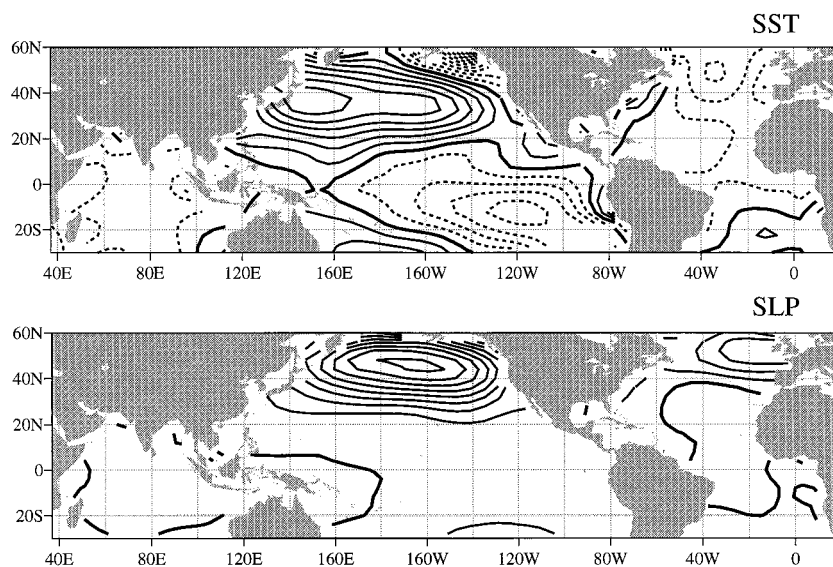


FIG. 15. Difference between time means: the epoch 1943–76 minus the previous epoch 1925–42. (top) The SST anomaly deviation field: contour interval 0.1 K. (bottom) The SLP field: contour interval 0.2 mb.

within the equatorial waveguide will increase the poleward and westward extent of the thermocline anomaly in the subtropical eastern basin and, hence, broaden the warming in this region. The distinctions in the SST anomaly patterns in Figs. 11 and 12 are qualitatively consistent with these inferences based on conventional notions of ENSO-related physics.

In all the fields shown in Figs. 11 and 12 the tropical features are more prominent in the ENSO cycle-related variability and the extratropical features, including the 500-mb height pattern in Fig. 13, are relatively more prominent in the residual variability. The residual 500-mb height pattern more closely resembles the most prominent mode of internal variability of the Northern Hemisphere wintertime geopotential height field (Wallace and Gutzler 1981; Barnston and Livezey 1987; Kushnir and Wallace

1989) and the leading mode of coupled variability of the extratropical Pacific SST and Northern Hemisphere geopotential height fields (Kawamura 1984; Lanzante 1984; Wallace et al. 1990, 1992). The emergence of this “Pacific–North American (PNA)” pattern in the residual variability is reminiscent of the coupled modeling results of Latif and Barnett (1994: their Figs. 1b and 3a).

Can the contrasting patterns in Figs. 11–14 be interpreted as being representative of interannual versus interdecadal variability or as contrasting “modes of variability”? As noted above, patterns qualitatively similar, in all respects, to those in Figs. 11–14 can be obtained using 6-yr highpass- and lowpass-filtered versions of G in Fig. 8 as reference time series. Hence, in distinguishing between these patterns, the labels “interannual” versus “interdecadal” are quite appropriate.

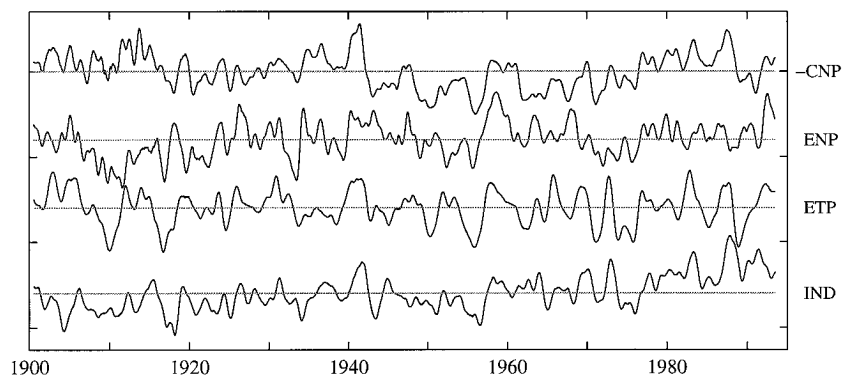


FIG. 16. Regional time series: SST anomalies averaged over the central North Pacific (CNP; 25°–50°N, 160°E–150°W; shown inverted), the eastern tropical Pacific (ENP; 25°–60°N, 135°–115°W), the eastern tropical Pacific (ETP; 20°N–20°S, east of the date line), the tropical Indian Ocean (IND; 20°N–20°S). All time series have been normalized and smoothed as in Fig. 8.

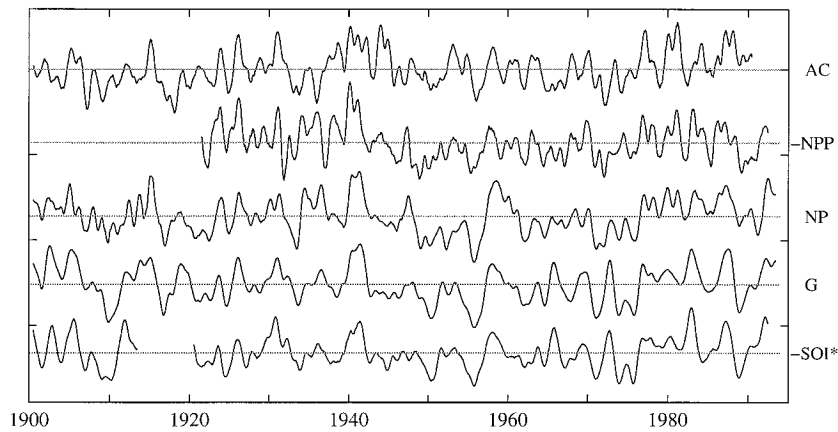


FIG. 17. Normalized time series: surface air temperature over Alaska and western Canada (AC; 50° – 70° N, 90° – 160° W); sea level pressure averaged over the central North Pacific (NNP; poleward of 30° N, 156° E– 138° W; shown inverted); NP and G, repeated from Fig. 8; and the COADS-based Southern Oscillation index (SOI*) as defined in section 2, shown inverted. The interval between tick-marks on the vertical axis is 1.0 std. The time series have been smoothed as in Fig. 8. The spacing between the curves is arbitrary.

However, we have intentionally refrained from referring to the contrasting patterns in Figs. 11–14 as statistically significant “modes of variability” in their own right. The 94-yr record analyzed in this study contains only a few realizations of the “ENSO-like interdecadal variations,” and even within this limited sample the correspondence between the interdecadal-scale features in regional time series is far from perfect. All that can be said with confidence is that the distinctions that we have drawn between the variability in the two frequency bands are representative of the major interdecadal and 5–10-yr swings in the historical record.

Is the above interpretation of the ENSO-like variability in the Pacific sector consistent with other observational studies? The present paper may be viewed as a sequel to our previous analysis (Zhang et al. 1996) of the relationship between the variability in the SST field over the Pacific Ocean and the Northern Hemisphere 500-mb height field, in which we showed evidence of coupling between the two fields, linearly independent of the ENSO cycle and consistent with the patterns in Fig. 11. To the extent that they can be compared, our EOFs are also generally consistent with those of Tanimoto et al. (1993), based on analysis of the time-filtered, extratropical North Pacific SST field.

It is difficult to compare the present study with those that have attempted to recover separate “modes” of variability using techniques such as conventional EOF analysis (Parker and Folland 1991; Miller et al. 1994; Deser and Blackmon 1995), rotated EOF analysis (Kawamura 1994), or Principal Oscillation Pattern analysis (Latif et al. 1997) because the interdecadal variability that we have identified exhibits a spatial signature that is similar, in so many respects, to that associated with the ENSO cycle. The confusion is exacerbated by the

general upward trend in global-mean SST over the century, which renders the results of conventional EOF analysis difficult to interpret. In view of these problems and the limited length of the historical record, we are not convinced that a formal modal separation involving interdecadal variability is meaningful.

Acknowledgments. We would like to thank Nathan Mantua for reading the manuscript and offering a number of helpful comments and suggestions. This work was supported by the National Science Foundation through the Climate Dynamics Program under Grant ATM 9215512 and a grant from the NOAA Climate and Global Change Program.

APPENDIX

Supplementary Correlation Statistics

TABLE A1. Correlation coefficients (in hundredths) between the 6-yr highpass-filtered cold tongue index (CT*); the five time series shown in Fig. 5; the conventional Darwin – Tahiti SLP Southern Oscillation index with sign inverted (–SOI); and the COADS-based Southern Oscillation index with sign inverted (–SOI*). Based on monthly mean data for the period 1950–93, smoothed with a 5-month running-mean filter, as in Fig. 5.

	CT*	CT	TP	G	G – TP	NP	–SOI
CT	94						
TP	84	94					
G	74	87	97				
G – TP	35	53	65	82			
NP	33	48	58	72	8		
–SOI	74	82	87	84	53	50	
–SOI*	68	81	89	91	70	67	87

TABLE A2. Correlation matrix for the time series in Figs. 8 and 10 plus the conventional Southern Oscillation index (SOI), and the COADS-based Southern Oscillation index (SOI*). Correlations (in hundredths) are based on the period of record 1900–93, except for those involving the SOI* for which the period July 1913–June 1920 is omitted due to insufficient data. All time series have been smoothed as in Fig. 8.

	CT*	CT	TP	G	GR	LG	G – TP	NP	–SOI
CT	91								
TP	81	93							
G	69	83	92						
GR	23	47	66	86					
LG	20	48	64	80	93				
G – TP	38	47	59	84	85	78			
NP	34	38	51	75	78	70	96		
–SOI	74	78	79	80	56	50	58	52	
–SOI*	71	84	89	89	70	68	62	55	82

TABLE A3. Average number of $5^{\circ} \times 5^{\circ}$ grid squares that enter into the calculation of monthly mean values of selected regional SST indices during various segments of the record, as indicated at left. The total number of grid boxes that lie within the region is indicated in the bottom row. ETP represents the eastern tropical Pacific (20°S – 20°N , 160°E – 80°W), IND the tropical Indian Ocean (20°S – 20°N , 40° – 120°E), CNP the central North Pacific (25° – 50°N , 160°E – 150°W), and ENP the eastern North Pacific (25° – 60°N , 135° – 115°W).

Year	ETP	IND	CNP	ENP
1900–15	57	76	13	17
1916–20	39	70	28	16
1921–40	82	85	37	21
1941–45	87	53	34	22
1946–60	121	67	30	21
1961–93	154	92	50	23
TOTAL	160	93	50	23

TABLE A4. Average number of $4^{\circ} \times 6^{\circ}$ grid squares that enter into the calculation of monthly mean values of the two poles of the COADS-based Southern Oscillation index SOI* during various segments of the record, as indicated at left. Each $4^{\circ} \times 6^{\circ}$ grid square comprises at least two $2^{\circ} \times 2^{\circ}$ grid squares. The total number of $4^{\circ} \times 6^{\circ}$ grid boxes that lie within the region is indicated in the bottom row. TAH* represents SLP averaged over the tropical (20°S – 20°N) Pacific from the dateline eastward, and DAR* represents SLP averaged over the remainder of the tropical oceans. NPP represents SLP averaged over the region poleward of 30°N , 156°E – 138°W .

Year	TAH*	DAR*	NPP
1900–6/1913	50	109	8
7/1913–6/1920	7	35	2
1921–40	71	175	43
1941–45	90	132	43
1946–60	139	254	66
1961–93	179	282	80
TOTAL	180	283	81

REFERENCES

- Alexander, M. A., 1992a: Midlatitude atmosphere–ocean interaction during El Niño. Part I: The North Pacific Ocean. *J. Climate*, **5**, 944–958.
- , 1992b: Midlatitude atmosphere–ocean interaction during El Niño. Part II: The Northern Hemisphere atmosphere. *J. Climate*, **5**, 959–972.
- Barnston, A., and R. E. Livezey, 1987: Classification, seasonality, and persistence of low-frequency circulation patterns. *Mon. Wea. Rev.*, **115**, 1083–1126.
- Battisti, D. S., and A. C. Hirst, 1989: Interannual variability in the tropical atmosphere–ocean system: Influence of the basic state, ocean geometry, and nonlinearity. *J. Atmos. Sci.*, **46**, 1687–1712.
- Bottomley, M., C. K. Folland, J. Hsiung, R. E. Newell, and D. E. Parker, 1990: *Global Ocean Surface Temperature Atlas (GOSTA)*. Her Majesty's Stationery Office, 20 pp. and 313 plates.
- Cayan, D. R., and D. H. Peterson, 1989: The influence of the North Pacific atmospheric circulation and streamflow in the west. *Aspects of Climate Variability in the Western Americas*, D. H. Peterson, Ed., Geophys. Monogr., No. 55, Amer. Geophys. Union, 375–397.
- Clarke, A. J., 1983: The reflection of equatorial waves from oceanic boundaries. *J. Phys. Oceanogr.*, **13**, 1193–1207.
- Davis, R. E., 1976: Predictability of sea surface temperature and sea level pressure anomalies over the North Pacific Ocean. *J. Phys. Oceanogr.*, **6**, 249–266.
- Deser, C., and J. M. Wallace, 1990: Large-scale atmospheric circulation features of warm and cold episodes in the tropical Pacific. *J. Climate*, **3**, 1254–1281.
- , and M. L. Blackmon, 1995: On the relationship between tropical and North Pacific sea surface temperature variations. *J. Climate*, **8**, 1677–1680.
- Dettinger, M. D., and D. R. Cayan, 1995: Large-scale atmospheric forcing of recent trends toward early snowmelt runoff in California. *J. Climate*, **8**, 606–623.
- Ebbesmeyer, C. C., D. R. Cayan, D. R. Mc Lain, F. H. Nichols, D. H. Peterson, and K. T. Redmond, 1991: 1976 step in the Pacific climate: Forty environmental changes between 1968–1975 and 1977–84. *Proc. Seventh Annual Pacific Climate (PACCLIM) Workshop*, Pacific Grove, CA, California Dept. of Water Resources, 115–126.
- Fletcher, J. O., R. J. Slutz, and S. D. Woodruff, 1983: Towards a comprehensive ocean–atmosphere dataset. *Trop. Ocean-Atmos. Newslett.*, **20**, 13–14.
- Folland, C. K., and D. E. Parker, 1990: Observed variations of sea surface temperature. *Climate–Ocean Interaction*, M. E. Schlesinger, Ed., Kluwer, 21–52.
- , and —, 1995: Correction of instrumental biases in historical sea surface temperature data. *Quart. J. Roy. Meteor. Soc.*, **121**, 319–367.
- Francis, R., and S. R. Hare, 1994: Decadal-scale regime shifts in the large marine ecosystems of the Northeast Pacific: A case for historical science. *Fish. Oceanogr.*, **3**, 179–291.
- Graham, N. E., 1994: Decadal-scale climate variability in the 1970s and 1980s: Observations and model results. *Climate Dyn.*, **10**, 135–162.
- Horel, J. D., and J. M. Wallace, 1981: Planetary-scale atmospheric phenomena associated with the Southern Oscillation. *Mon. Wea. Rev.*, **109**, 813–829.
- Hsuing, J., and R. E. Newell, 1983: The principal nonseasonal modes of global sea surface temperature. *J. Phys. Oceanogr.*, **13**, 1957–1967.
- Jones, P. D., and Coauthors, 1985: A grid point temperature data set for the Northern Hemisphere. U.S. Dept. of Energy, Carbon Dioxide Research Division, Tech. Rep. TR022, 251 pp. [NTIS 85015609.]
- Kawamura, R., 1984: Relation between atmospheric circulation and dominant sea surface temperature anomaly patterns in the North Pacific during the Northern winter. *J. Meteor. Soc. Japan*, **62**, 910–916.
- , 1994: A rotated EOF analysis of global sea surface temperature variability with interannual and interdecadal scale. *J. Phys. Oceanogr.*, **24**, 707–715.
- Kushnir, Y., and J. M. Wallace, 1989: Low frequency variability in

- the Northern Hemisphere winter: Geographical distribution structure and time-scale. *J. Atmos. Sci.*, **46**, 3122–3142.
- Lanzante, J. R., 1984: A rotated eigenanalysis of the correlation between 700 mb heights and sea-surface temperatures in the Pacific and Atlantic. *Mon. Wea. Rev.*, **112**, 2270–2280.
- Latif, M., and T. P. Barnett, 1994: Causes of decadal climate variability over the North Pacific/North American sector. *Science*, **226**, 634–637.
- , A. Sterl, E. Maier-Reimer, and M. M. Junge, 1993: Climate variability in a coupled GCM. Part I: The tropical Pacific. *J. Climate*, **6**, 5–21.
- , R. Kleeman, and C. Eckert, 1997: Greenhouse warming, decadal variability, or El Niño? An attempt to understand the anomalous 1990s. *J. Climate*, in press.
- Miller, A. J., D. R. Cayan, T. P. Barnett, N. E. Graham, and J. M. Oberhuber, 1994: Interdecadal variability of the Pacific Ocean: Model response to observed heat flux and wind stress anomalies. *Climate Dyn.*, **9**, 287–302.
- Nitta, T., and S. Yamada, 1989: Recent warming of tropical sea surface temperature and its relationship to the Northern Hemisphere circulation. *J. Meteor. Soc. Japan*, **67**, 187–193.
- North, G. R., T. L. Bell, and R. F. Cahalan, 1982: Sampling errors in the estimation of empirical orthogonal function. *Mon. Wea. Rev.*, **110**, 669–706.
- Parker, D. E., and C. K. Folland, 1991: Worldwide surface air temperature trends since the mid-19th century. *Greenhouse-Gas Induced Climatic Change: A Critical Appraisal of Simulations and Observations*, M. E. Schlesinger, Ed., Elsevier, 173–193.
- Quinn, W. H., and V. T. Neal, 1984: Recent climate change and the 1982–83 El Niño. *Proc. Eighth Annual Climate Diagnostic Workshop*, Downsview, ON, Canada, NOAA, 148–154.
- , and —, 1985: Recent long-term climate change over the eastern tropical and subtropical Pacific and its ramifications. *Proc. Ninth Annual Climate Diagnostic Workshop*, Corvallis, OR, NOAA, 101–109.
- Rasmusson, E. M., and T. H. Carpenter, 1982: Variations in tropical sea surface temperature and surface wind fields associated with the Southern Oscillation/El Niño. *Mon. Wea. Rev.*, **110**, 1103–1113.
- Schneider, E. K., B. Huang, and J. Shukla, 1995: Ocean wave dynamics and El Niño. *J. Climate*, **8**, 2415–2439.
- Shriver, J. F., and J. J. O'Brien, 1995: Low-frequency variability of the equatorial Pacific Ocean using a new pseudostress dataset: 1930–1989. *J. Climate*, **8**, 2762–2786.
- Tanimoto, Y., N. Iwasaka, K. Hanawa, and Y. Toba, 1993: Characteristic variations of sea surface temperature with multiple time scales in the North Pacific. *J. Climate*, **6**, 1153–1160.
- Tokioka, T., A. Noda, A. Kitoh, Y. Nakaidou, S. Nakagawa, T. Motoi, S. Yukimoto, and K. Takata, 1995: A transient CO₂ experiment with the MRI CGCM—Quick report. *J. Meteor. Soc. Japan*, **73**, 817–826.
- Trenberth, K. E., 1990: Recent observed interdecadal climate changes in the Northern Hemisphere. *Bull. Amer. Meteor. Soc.*, **71**, 988–993.
- , and J. W. Hurrell, 1994: Decadal atmospheric–ocean variations in the Pacific. *Climate Dyn.*, **9**, 303–309.
- Troup, A. J., 1965: The Southern Oscillation. *Quart. J. Roy. Meteor. Soc.*, **91**, 490–506.
- Wallace, J. M., and D. S. Gutzler, 1981: Teleconnections in the geopotential height field during the Northern Hemisphere winter. *Mon. Wea. Rev.*, **109**, 784–812.
- , C. Smith, and Q. Jiang, 1990: Spatial patterns of atmosphere–ocean interaction in the Northern winter. *J. Climate*, **3**, 990–998.
- , —, and C. S. Bretherton, 1992: Singular value decomposition of wintertime sea-surface temperature and 500 mb height anomalies. *J. Climate*, **5**, 561–576.
- Wang, B., 1995: Interdecadal changes in El Niño onset in the last four decades. *J. Climate*, **8**, 267–285.
- Weare, B., A. Navato, and R. E. Newell, 1976: Empirical orthogonal analysis of Pacific Ocean sea surface temperature. *J. Phys. Oceanogr.*, **6**, 671–678.
- Webster, P. J., 1982: Seasonality in the local and remote atmospheric response to sea surface temperature anomalies. *J. Atmos. Sci.*, **38**, 554–571.
- Yukimoto, S., M. Endoh, Y. Kitamura, A. Kitoh, T. Motoi, A. Noda, and T. Tokioka, 1996: Interannual and interdecadal variabilities in the Pacific in an MRI coupled GCM. *Climate Dyn.*, **12**, 667–683.
- Yulaeva, E., and J. M. Wallace, 1994: The signature of ENSO in global temperature and precipitation fields derived from the microwave sounding unit. *J. Climate*, **7**, 1720–1736.
- Zhang, Y., J. M. Wallace, and N. Iwasaka, 1996: Is climate variability over the North Pacific a linear response to ENSO? *J. Climate*, **9**, 1468–1478.